optica

High-power 100 fs semiconductor disk lasers

Dominik Waldburger,[1,*] Sandro M. Link,[1] Mario Mangold,[1] Cesare G. E. Alfieri,[1] Emilio Gini,[2] Matthias Golling,[1] Bauke W. Tilma,[1] and Ursula Keller[1]

[1]Department of Physics, Institute for Quantum Electronics, ETH Zürich, 8093 Zürich, Switzerland
[2]FIRST Center for Micro- and Nanoscience, ETH Zürich, 8093 Zürich, Switzerland
*Corresponding author: dominikw@phys.ethz.ch

Received 2 May 2016; revised 29 June 2016; accepted 1 July 2016 (Doc. ID 264259); published 29 July 2016

Optically pumped passively modelocked semiconductor disk lasers (SDLs) provide superior performance in average output power, a broad range of operation wavelengths, and reduced complexity. Here, we present record performance with high average power and pulse durations as short as 100 fs with a semiconductor saturable absorber mirror (SESAM) modelocked vertical external-cavity surface-emitting laser (VECSEL) at a center wavelength of 1034 nm. A comprehensive pulse characterization confirms fundamental modelocking with a close to transform-limited output pulse of 128 fs and with negatively chirped output pulses as short as 107 fs, which are externally compressed to 96 fs with a single path through a 2-mm-thick ZnSe plate. For the "96 fs result" the pulse repetition rate is 1.6 GHz, the average output power is 100 mW, and the pulse peak power is 560 W. The transform-limited optical spectrum could in principle support pulses as short as 65 fs with higher order dispersion compensation. We measured the most relevant spectral and nonlinear VECSEL and SESAM parameters and used them as input parameters for our pulse formation simulations. These simulations agree well with our experimental results and provide an outlook for further performance scaling of ultrafast SDL technology.

OCIS codes: (140.3460) Lasers; (140.4050) Mode-locked lasers; (140.5960) Semiconductor lasers; (140.7090) Ultrafast lasers; (140.7270) Vertical emitting lasers.

http://dx.doi.org/10.1364/OPTICA.3.000844

1. INTRODUCTION

Passive modelocking of optically pumped semiconductor disk lasers (SDLs) [1] using semiconductor saturable absorber mirrors (SESAMs) [2] has demonstrated impressive progress during the past 10 years, as reviewed recently [3]. The optically pumped vertical external-cavity surface-emitting laser (VECSEL) [4] was the first laser in the family of semiconductor disk lasers to demonstrate significant power scaling by superior heat removal in a thin disk geometry. The optically pumped VECSEL is an efficient mode converter that uses low-coherent high-power diode pump arrays and benefits from semiconductor bandgap engineering to support emission wavelengths ranging from UV to mid-IR (i.e., 391 nm up to 5.3 μm) [5,6]. The highest continuous wave (cw) output power is ≈20 W in a Gaussian mode profile [7–9] and 106 W in multimode operation [10] at an emission wavelength around ≈1 μm using InGaAs quantum well gain on GaAs/AlGaAs Bragg reflectors. Here, we present record power performance with SESAM-modelocked VECSELs generating pulse durations in the 100 fs regime (Fig. 1).

We have observed a strong trade-off between short pulse durations and average power or pulse peak power (Fig. 1). Fundamental physical processes, such as non-equilibrium kinetic hole burning [12], can partially explain this, but the full complex interplay between the gain and absorber dynamics in these high-Q SDLs are not yet fully understood. To date, the shortest pulses have been 107 fs, but with only 3 mW of average output power [13] and 60 fs in a pulse train within a picosecond pulse envelope [14]. The highest pulse peak power of up to 4.35 kW was obtained with significantly longer pulses of 400 fs duration [15].

Peak power scaling by reducing the pulse repetition rate has been successfully demonstrated with diode-pumped solid-state lasers [16]. This approach is less attractive for diode-pumped semiconductor lasers because the highly inverted quantum well gain has a lifetime of only a few hundred picoseconds, which currently limits the pulse repetition rate of quantum well VECSELs to above 100 MHz without the use of a more elaborated multi-gain-pass cavity [17,18]. Quantum dot gain SDLs [19–21] have a longer upper-state lifetime and may offer better performance in the future.

Many applications greatly benefit from a combination of femtosecond pulses with high pulse peak power to drive nonlinear optical processes, such as two-photon absorption for multiphoton microscopy [22] or supercontinuum generation for frequency comb applications [23–25]. The standard method to detect and stabilize the carrier-envelope offset (CEO) frequency in a self-referencing scheme is based on f-to-2f interferometry [26], for which a coherent octave spanning spectrum is required. Typically the combination of sub-100-fs pulses with kilowatt

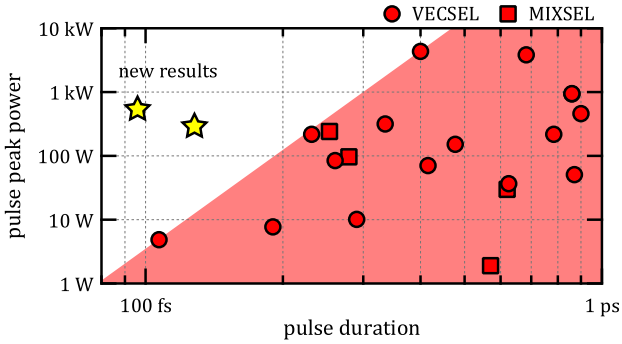

Fig. 1. Overview of the pulse peak power versus pulse duration of the state-of-the-art femtosecond SDLs operating at a center wavelength around 1 μm using InGaAs gain layers [3,11]. The yellow stars indicate the two new milestone results presented in this paper.

pulse peak power was required for coherent supercontinuum generation in photonic crystal fibers [27], but supercontinuum generation in silicon nitride waveguides strongly reduces this requirement [28].

The limited upper-state lifetime of semiconductor lasers makes them ideally suited for gigahertz pulse repetition rates and the high gain cross-section eliminates *Q*-switching instabilities, typically a challenge with SESAM-modelocked diode-pumped ion-doped solid-state lasers [29,30]. The gigahertz repetition rate can be beneficial for frequency comb applications, since the comb lines have a larger frequency spacing with more power per mode and therefore provide a better signal-to-noise ratio (SNR). Additional benefits are a faster data acquisition or a faster data transmission in telecommunication applications [31]. To date, ultrafast SDLs have been demonstrated up to 100 GHz [32].

Here, we present two new milestone results for femtosecond ultrafast SDLs (shown in yellow in Fig. 1). First, our "128 fs result" with a pulse duration of 128 fs, a pulse repetition rate of 1.8 GHz, an average power of 80 mW, and, therefore, a pulse peak power of 303 W, slightly improved compared to [33]. Second, we present our "96 fs result" with a pulse duration of 96 fs, a pulse repetition rate of 1.6 GHz, an average power of 100 mW, and, therefore, a pulse peak power of 560 W. These are, to the best of our knowledge, the shortest pulses of a fundamental modelocked SDL. To achieve pulse duration of 96 fs, the slightly negatively chirped 107 fs output pulses have been compressed with a single path through a 2-mm-thick zinc selenide plate.

We used a newly optimized VECSEL structure following the guidelines based on numerical pulse formation simulations [34]. This VECSEL structure has a larger gain saturation fluence and a slightly positive but flat group delay dispersion (GDD) over a larger gain bandwidth. In addition, a fast SESAM with a low saturation fluence was required. In a similar approach Head *et al.* [35] presented preliminary results of a high-power sub-200-fs VECSEL. We did not include this result in our overview graph because the VECSEL chip got damaged before fundamental modelocking was confirmed. Higher average power can easily be obtained with multiple pulses per cavity round-trip.

We measured most laser and absorber parameters (Table 1) [36,37], which were used as input parameters for our numerical pulse formation simulation and obtained a good agreement. This allows us to give an outlook for further performance scaling at the end of this paper.

2. LASER DESIGN

The laser cavity is arranged in a simple V-shaped cavity where the output coupler and the SESAM form the end mirrors, and the VECSEL chip is used as a folding mirror, as shown in Fig. 2. For the "96 fs result" [Fig. 2(a)], we changed the V-shaped cavity such that we more strongly saturate the absorber (i.e., beam radius in the gain estimated from ABCD-matrix calculations is increased from 186 to 192 μm, and in the absorber the beam radius is decreased from 100 to 83 μm; Table 1) and obtained more balanced cavity legs L_1 and L_2 (Fig. 2), which is clearly preferred for better gain recovery. In addition, for the "96 fs result," we inserted a 1-mm-thick fused silica Brewster plate (Infrasil 302, 30′ wedged; wzw-optic AG) between the VECSEL and the SESAM for more stable operation in linear polarization and shorter pulses. The wedged plate strongly reduces etalon effects and introduces additional positive dispersion inside the cavity. The VECSEL is pumped under an angle of 45° with a 35 W, 808 nm spatial multimode diode laser (LIMO; Lissotschenko Mikrooptik GmbH), with an elliptical shaped beam such that on the VECSEL chip surface the pump beam is circular with a radius of 177 μm. For the "96 fs result" we used a pump power of 21 W and for the "128 fs result" we used 18.1 W. The VECSEL and the SESAM are temperature stabilized with water-cooled Peltier elements to 1°C (−10°C) and 37°C (24°C), respectively for the "96 fs result" ("128 fs result").

A. VECSEL

The VECSEL structure was grown on a metalorganic vapor phase epitaxy (MOVPE) machine. For flip-chip bonding, the structure was grown in reversed order on a 600-μm-thick, (100)-oriented GaAs substrate. The structure is divided into a distributed Bragg reflector (DBR), an active region, and a multipurpose antireflection (AR) top coating, as shown in Fig. 2(c). The active region is

Table 1. Complete List of Input Parameters Used for the Pulse Formation Simulation[a]

Cavity		VECSEL		SESAM	
Output coupler	0.9%	Saturation fluence	40 μJ/cm^2	Saturation fluence	4.3/5.4 μJ/cm^2
Other losses	0.8%	*Recovery time*	3 ns	Fast recovery time	560 fs
Repetition rate	1.63/1.81 GHz	*Linewidth enhancement factor*	3	Slow recovery time	5.5 ps
Center wavelength	1034/1033 nm	Small signal gain	2.9%	Amplitude of slow component	0.25
Round-trip GDD	−12/12 fs^2	Gain FWHM	50 nm	*Linewidth enhancement factor*	2
Round-trip TOD	−500/620 fs^3	*Beam radius*	192/185 μm	Modulation depth	2.03/1.37%
				Beam radius	83/100 μm

[a]All non-italic parameters have been directly measured. If different, we show the parameters for the two modelocking results as follows: 96 fs input parameter/128 fs input parameter.

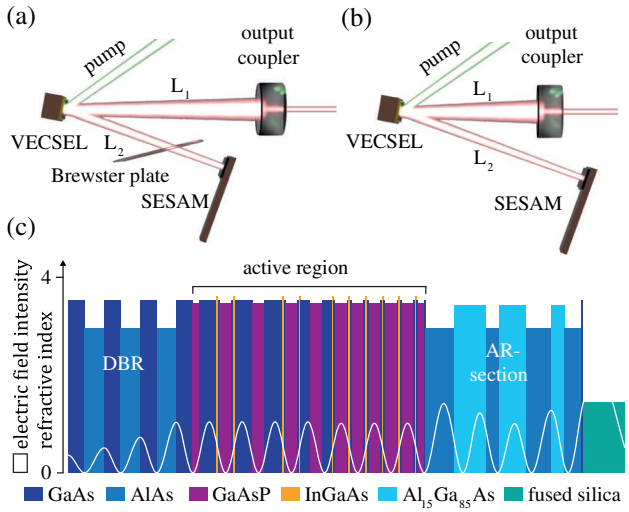

Fig. 2. V-shaped cavity design with SESAM and output coupler as end mirrors and the VECSEL gain chip as a folding mirror. The output coupler has a 0.9% transmission and a radius of curvature of 100 mm. The folding angle is 20°. The 1-mm-thick fused silica Brewster plate was only used for the "96 fs result." (a) Cavity for the "96 fs result": $L_1 = 4.8$ cm and $L_2 = 4.2$ cm. (b) Cavity for the "128 fs result": $L_1 = 3.4$ cm and $L_2 = 4.8$ cm. (c) VECSEL layer stack, with a DBR, a strain-compensated active region with 10 InGaAs quantum wells, and a multi-purpose AR section. The center laser wavelength is designed to be 1030 nm, and the white curve indicates the corresponding standing electric field intensity (normalized to 4 outside the structure).

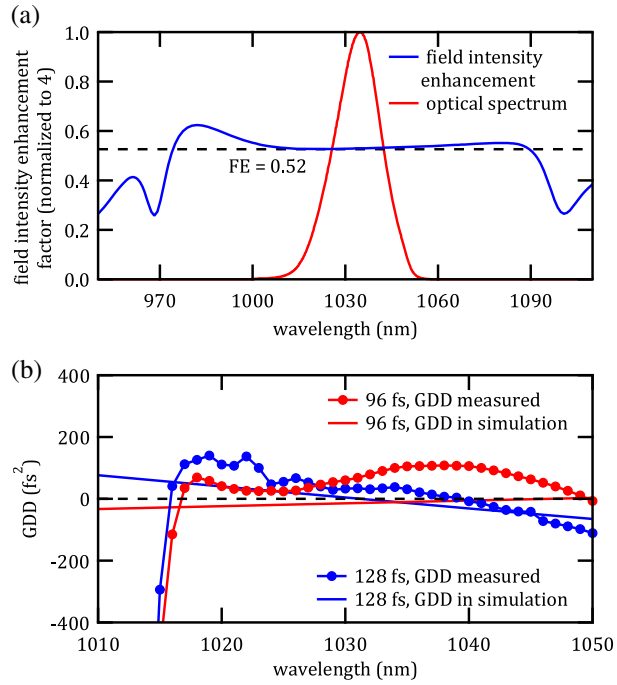

Fig. 3. (a) Average field intensity in the gain quantum wells of the VECSEL (blue) normalized to the incoming field intensity (i.e., a 100% reflector results in a field intensity of 4) and the measured optical spectrum (red). (b) Measured GDD of the "unpumped" VECSEL structure at normal incidence and at room temperature (circles). For simulation of the modelocking results, we used the dispersion (both second and third order) as an adjustable parameter (Table 1). The dispersion explaining our pulse durations is shown for the "128 fs result" (blue line) and the "96 fs result" (red line).

grown at a lower substrate temperature of 660°C, while the DBR and the AR top coating are grown at 750°C.

The DBR consists of 23.5 pairs of GaAs/AlAs quarter-wave layers, which balances the trade-off between sufficient DBR reflectivity and high thermal conductivity to the underlying heat spreader. The center wavelength is designed to be at 1030 nm.

The active region contains five pairs of strain-compensated InGaAs quantum wells. The compressively strained, 8.8-nm-thick $In_{0.193}Ga_{0.807}As$ quantum wells are embedded in GaAs and compensated by 54 nm tensile strained $GaAs_{0.933}P_{0.067}$ layers. The quantum well pairs are separated by 64 nm and are placed symmetrically around the node or the anti-node of the standing electric field intensity. The spacing is optimized to obtain a low and spectrally flat field intensity enhancement factor of 0.52 [Fig. 3(a)]. The field intensity enhancement factor is defined as the field intensity inside the quantum wells averaged over all quantum wells and is normalized to the incoming field intensity (i.e., a 100% reflector results in a field intensity of 4) [38]. The spectrally flat field intensity enhancement avoids structural gain bandwidth restrictions, and the lower field intensity enhancement is expected to increase the gain saturation fluence at the expense of available gain. The pump absorbing GaAs layers become thicker with increasing penetration of the pump light [Fig. 2(c)], and the AR coating is designed for no absorption. The AR section consists of 3.5 pairs of $Al_{0.15}Ga_{0.85}As$/AlAs followed by a fused SiO_xN_y dielectric layer and is optimized for a reduced pump reflectivity, a broadband flat GDD, and a close to zero but positive GDD.

The semiconductor structure is cleaved in 4.5 mm × 4.5 mm pieces and is then flip-chip bonded onto a 1-mm-thick chemical vapor deposited diamond heat spreader with a high thermal conductivity exceeding 2000 $W\,m^{-1}\,K^{-1}$ [39]. After soldering and wet etching, the final SiO_xN_y layer is deposited using plasma-enhanced chemical vapor deposition (PECVD; Oxford Instruments).

The two modelocking results have been achieved with chips from different processing runs resulting in different SiO_xN_y layer thicknesses and so different GDD. The GDD of the VECSELs is measured at 20°C without optical pumping [40]. The measured GDD curves [Fig. 3(b)] are not flat but have in comparison to prior results [23] a much smaller deviation of ± 100 fs^2. The drop in GDD at 1015 nm is due to the absorption of the quantum wells. The nonuniform PECVD deposition allows us to further optimize the GDD by scanning the position on the processed chip.

B. SESAM

The SESAM was grown on a molecular beam epitaxy (MBE) machine. A single InGaAs quantum well absorber is grown on top of a 30 pair GaAs/AlAs DBR. To achieve a fast recovery time, the absorber is grown at a low temperature of 260°C and is embedded in AlAs barriers. The field intensity enhancement factor of the antiresonant structure can be engineered by PECVD deposition of a SiN_x top coating. An increased field intensity enhancement gives rise to a lower saturation fluence and an increased modulation depth [38]. For the "96 fs results," we reduced the mode size for a stronger saturation and increased the modulation depth with a higher temperature (i.e., moving from a heat-sink

temperature of 24°C to 37°C). All SESAM parameters are summarized in Table 1.

3. MODELOCKING RESULT

A careful and extended pulse characterization has to be performed to prove clean and stable fundamental modelocking. An incomplete or limited characterization may incorrectly suggest fundamental modelocking and may result in much higher average output powers [11]. In the following, the two modelocking results are presented. For the "96 fs result," the initially negatively chirped 107 fs output pulses are externally compressed by a single path through a 2-mm-thick zinc selenide plate (Eksma Optics) introducing a positive GDD of ≈1350 fs^2.

The detailed pulse characterization is summarized in Figs. 4 and 5. The pulse duration is measured with a home-built second harmonic generation (SHG) frequency-resolved optical gating (FROG) apparatus. The measured SHG-FROG spectrogram is reconstructed with a grid size of 512 by 512 points [Fig. 4(a)] and 1024 by 1024 points [Fig. 5(a)]. The retrieved pulse durations agree well with a more standard SHG-based autocorrelator (FR-103MN; Femtochrome Research, Inc.). The intensity autocorrelations are in excellent agreement with a $sech^2$ pulse shape [Figs. 4(d) and 5(d)], and long-span autocorrelation scans show no additional side pulses or pedestals [inset in Figs. 4(d) and 5(d)]. Figure 5(d) shows the autocorrelation of both the 107 fs output pulses and the compressed 96 fs pulses. The following pulse characterizations are identical for the 107 fs and the 96 fs pulses. The smooth modelocked spectrum overlaps with the retrieved FROG spectrum [Figs. 4(e) and 5(e)] and is free of cw breakthroughs, further shown in a logarithmic scale in Figs. 4(f) and 5(f). The "128 fs result" is close to transform-limited with a spectral bandwidth of 9.48 nm corresponding to a time–bandwidth product of 0.345, being 1.09 times the value for a $sech^2$ pulse shape. The 17.5 nm broad spectrum of the "96 fs result" corresponds to a time–bandwidth product of 0.472, i.e., 1.47 times the ideal value for a $sech^2$ pulse shape, and better external pulse compression could potentially support pulses as short as 65 fs.

The temporal laser intensity is measured with a fast photodiode (New Focus, Model 1454), amplified with a broadband and low noise preamplifier (Agilent 87405C) and detected with a microwave spectrum analyzer (Agilent 8565EC, HP 8592L). As discussed in [11], we show two microwave spectra in Figs. 4(g), 5(g) and Figs. 4(h), 5(h) to further confirm clean fundamental modelocking.

Figures 4(g) and 5(g) show a scan with high resolution bandwidth (RBW) of 300 kHz from DC to 22 GHz with a high SNR of ≈50 dB. All higher harmonics of the repetition rate exist and are constant, apart from a small drop in intensity of the higher harmonics due to the limited bandwidth of the 18 GHz preamplifier. Figures 4(h) and 5(h) zoom into the first harmonic with a higher RBW over an offset frequency span of ±7.5 MHz using a highly linear photodiode (DSC30S-HLPD; Discovery Semiconductors, Inc.) and a signal source analyzer (Agilent E5052B). Even with the high SNR of ≈80 dB (≈90 dB), no line

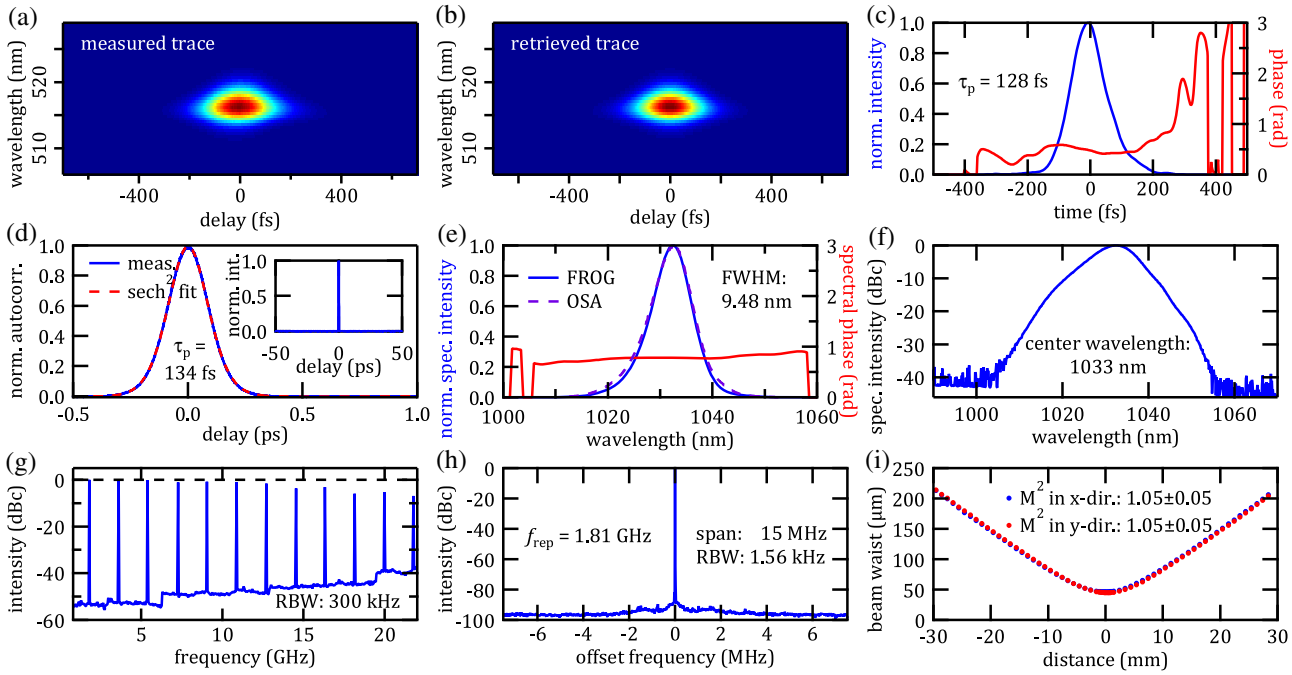

Fig. 4. "128 fs result": modelocking characterization of the 128 fs pulses at 80 mW average output power, a peak power of 303 W, and a pulse repetition rate of 1.81 GHz. (a) Measured SHG-FROG spectrogram. (b) Retrieved FROG spectrogram (error: 0.0019). (c) Retrieved temporal intensity profile and temporal phase. (d) Intensity autocorrelation with corresponding $sech^2$ fit (inset: long-span autocorrelation without any satellite pulses). (e) Retrieved spectrum and spectral phase overlaid with the measured optical spectrum with a FWHM bandwidth of 9.48 nm. The time–bandwidth product is 1.09 times the ideal value for a $sech^2$ pulse shape, i.e., very close to perfect bandwidth-limited pulse duration. (f) Optical spectrum in logarithmic scale centered around 1033 nm, measured with a RBW of 0.1 nm. (g) Long-span microwave spectrum with a RBW of 300 kHz. (h) 15 MHz microwave spectrum at 1.81 GHz, measured with a RBW of 1.56 kHz. (i) Gaussian beam profile confirmed with a measured $M^2 < 1.05 \pm 0.05$ in two orthogonal directions.

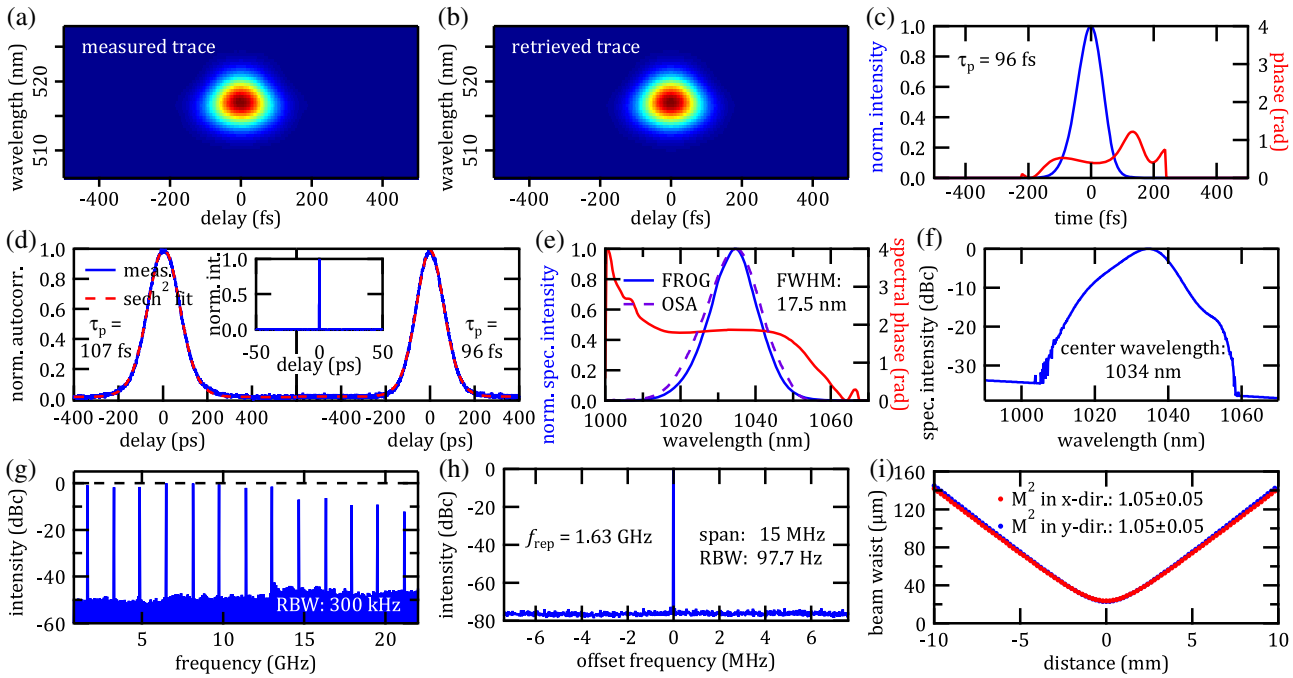

Fig. 5. "96 fs result": modelocking characterization of the 96-fs pulses at 100 mW average output power, a peak power of 560 W and a pulse repetition rate of 1.63 GHz. (a) Measured SHG-FROG spectrogram. (b) Retrieved FROG spectrogram (error: 0.0004). (c) Retrieved temporal intensity profile and temporal phase. (d) Intensity autocorrelations with corresponding sech^2 fits of the 107 fs and 96 fs pulses (inset: long-span autocorrelation without any satellite pulses). (e) Retrieved spectrum and spectral phase overlaid with the measured optical spectrum with a FWHM bandwidth of 17.5 nm. The time–bandwidth product is 1.47 times the ideal value for a sech^2 pulse shape, i.e., with better dispersion compensation, we could obtain even shorter pulses. (f) Optical spectrum in logarithmic scale centered around 1034 nm, measured with a RBW of 0.1 nm. (g) Long-span microwave spectrum with a RBW of 300 kHz. (h) 15 MHz microwave spectrum at 1.63 GHz, measured with a RBW of 97.7 Hz. (i) Gaussian beam profile confirmed with a measured $M^2 < 1.05 \pm 0.05$ in two orthogonal directions.

broadening and no additional side peaks become visible. Excellent beam quality was confirmed with measured M^2 values of less than 1.05 ± 0.05 in two orthogonal directions [Figs. 4(i) and 5(i)].

4. GAIN CHARACTERIZATION

Here we present both a spectrally resolved measurement of the small signal gain and a measurement of the gain saturation as described by Mangold *et al.* [37].

A. Spectral Gain Measurements

For the spectral gain characterization, we measured the spectrally resolved small signal reflectivity of a diode-pumped VECSEL. The probe laser is a tunable cw Ti:sapphire laser that is focused tightly to obtain a sub-20-μm diameter beam waist on the surface of the VECSEL chip. The VECSEL is optically pumped by a cw 808 nm multimode diode laser (Lumics) with an elliptical 122 μm × 172 μm full width at half-maximum (FWHM) spot. The average pump intensity I_p of the probe spot can be varied from 0 to 57 kW/cm^2. Without any pump power, the VECSEL absorbs the probe laser for photon energies exceeding the bandgap energy [Fig. 6(a)]. With a pump intensity of approximately 10 kW/cm^2, the laser is pumped into transparency. For increasing pump power, the small signal gain increases, the spectrum becomes broader, and the peak wavelength experiences a redshift due to the elevated temperature in the gain quantum wells.

A shift in the peak wavelength is also visible in Fig. 6(b), which shows the small signal gain for different heat-sink temperatures at a constant pump intensity of 57 kW/cm^2. By lowering the heat-sink temperature, the small signal gain increases slightly, and the peak wavelength experiences a blueshift in the range

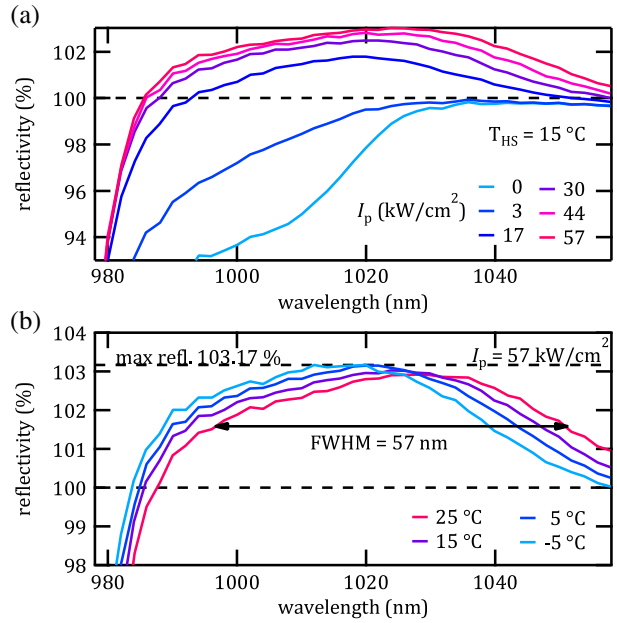

Fig. 6. Spectral gain measurements. (a) Spectrally resolved reflectivity for different pump intensities at a constant heat-sink temperature of 15°C. (b) Spectrally resolved reflectivity for different heat-sink temperatures at a constant pump intensity of $I_p = 57$ kW/cm^2.

of 0.32 nm/K, in agreement with the intrinsic temperature dependence of the InGaAs quantum well gain [1]. The maximum small signal gain of 3.17% is achieved at 57 kW/cm^2 pump intensity and a heat-sink temperature of −5°C. The small signal gain is lower than the values measured in [37], which can be explained by the reduced field intensity enhancement factor.

The VECSEL chip is heated by the absorbed pump light from the front side and cooled from the backside, creating a temperature gradient normal to the chip surface. This temperature gradient in the active region leads to different temperatures of the individual quantum wells, which shifts the corresponding emission wavelength and thereby broadens the overall accessible macroscopic gain. This effect becomes even stronger with increased pump intensities and reduced heat-sink temperatures. The short wavelength limit of the gain shown in Fig. 6, is defined by the reflectivity bandwidth of the underlying AlAs/GaAs DBR (full bandwidth of about 110 nm), resulting in a gain bandwidth of approximately 50–57 nm. This corresponds to a small signal gain, which is 2–3 times broader than the quantum well photoluminescence measured by Wang *et al.* [7].

B. Gain Saturation Measurements

For the gain saturation characterization, we measured the fluence-dependent reflectivity of the diode-pumped VECSEL. The probe laser is a tunable modelocked Ti:sapphire laser generating 140 fs pulses. The probe light is focused to a 29.6 μm diameter spot. The pump arrangement is the same as the one used for the spectral gain measurement, resulting in a maximum pump intensity of 46.5 kW/cm^2. The dependence of the reflectivity on the probe fluence is measured for different probe wavelengths, pump fluences, and heat-sink temperatures. The probe fluence is varied over 3 orders of magnitude up to 1200 μJ/cm^2 for probing wavelengths of 1010, 1020, 1030, and 1040 nm. The pump intensity is varied between 0 and 46.5 kW/cm^2, while the heat-sink temperature is kept at −5°C, 5°C, 15°C, or 25°C.

The nonlinear reflectivity [Fig. 7(a)] is analyzed with a macroscopic model for the gain saturation analogous to the saturable absorption of a SESAM. The characteristic parameters are the small signal reflectivity, the gain saturation fluence, the nonsaturable losses, and the induced absorption. The detailed description of the model can be found in [37].

To study the measured gain saturation parameters, the concept of the equivalent wavelength is introduced, which allows for a matching of measurement series taken at different probing wavelengths and temperatures. As visible in Fig. 6(b), the quantum well emission is blueshifted by approximately 3.2 nm for a heat-sink temperature reduction of 10°C. To account for this blueshift, the probing wavelength of 1030 nm at a heat-sink temperature of 15°C corresponds to an equivalent probing wavelength of 1033.2 nm at a heat-sink temperature of 25°C, for example. Following this concept, the equivalent probing wavelength is calculated for all temperatures lower than 25°C.

The saturation fluence varies between 30 and 50 μJ/cm^2 and has a slight dip around 1030 nm [Fig. 7(b)]. The saturation fluence is comparable to that reported in [37], although the saturation fluence is expected to scale inversely proportional to the field intensity enhancement factor, and, therefore, we have expected higher saturation fluences. Figure 7(c) shows the small signal reflectivity of the probing pulse with an 11 nm wide spectrum analogous to the reflectivity spectrum [Fig. 6(b)] of a single frequency cw probe. The small signal reflectivity has a maximum around 1030 nm and is slightly reduced for lower heat-sink temperatures. The induced absorption shows a weak temperature dependence and has a maximum of 17.6 mJ/cm^2 at a probing wavelength of 1030 nm, as shown in Fig. 7(d).

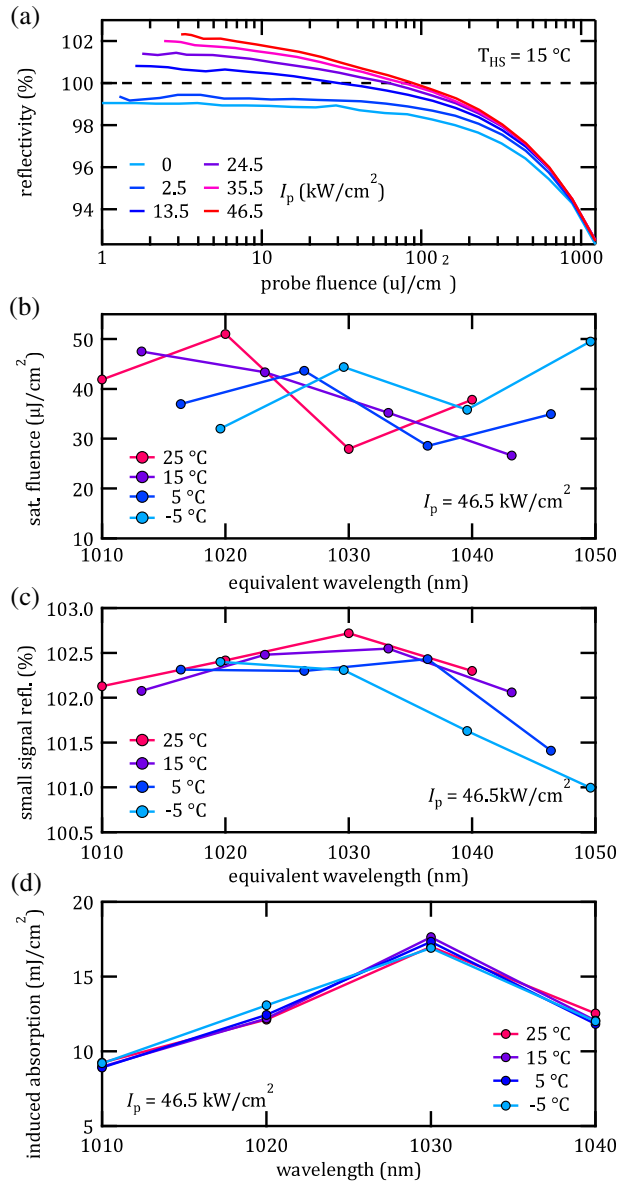

Fig. 7. Gain saturation measurements. (a) Fluence-dependent reflectivity for different pump intensities at a heat-sink temperature of 15°C. (b) Saturation fluence as a function of heat-sink temperature and equivalent wavelength. (c) Small signal reflectivity as a function of heat-sink temperature and equivalent wavelength. The equivalent wavelength accounts for the temperature-induced wavelength shift of the gain peak wavelength for matching of measurement series. See text for a more detailed definition of equivalent wavelength. (d) Induced absorption as a function of wavelength and heat-sink temperature.

5. PULSE FORMATION SIMULATION

We used our pulse formation simulations as described in [34]. This simulation is based on macroscopic input parameters summarized in Table 1. We used the same linewidth enhancement

factors, the same additional cavity losses, and the same gain recovery time as discussed before in [34]. The input parameters of the VECSEL gain chip are chosen in the middle of the measured range of 50–57 nm (FWHM) for the gain bandwidth, 30–50 μJ/cm^2 for the gain saturation fluence, and 2.5%–3.17% for the small signal gain. More elaborated simulations starting from the fully microscopic many-body theory by Kilen *et al.* [41] indicated the limitations of macroscopic models for pulse durations below some hundreds of femtoseconds. Nevertheless, so far our macroscopic models have shown good agreement with our experimental results.

Our simulation shows that the combination of the gain bandwidth [Fig. 6(b)] and the gain saturation fluence [Fig. 7(b)] defines a range of stable modelocking configurations and, so, the minimum possible pulse duration. As expected, the small signal gain [Fig. 6(b)] and the losses mainly determine the output power. The values for dispersion per cavity round-trip used for the simulation are not straightforward because, for example, the dispersion of the VECSEL [Fig. 3(b)] was not measured under lasing operation. Furthermore, the modelocking simulations are very sensitive to dispersion, with increasing sensitivity for increasing gain bandwidth. The cavity round-trip dispersion fitting the "96 fs result" is −12 fs^2 of GDD and −500 fs^3 of third-order dispersion (TOD), and these values are 12 fs^2 of GDD and 620 fs^3 of TOD for the "128 fs result." These dispersion values are shown in Fig. 3(b) and are in reasonable agreement with the dispersion of the VECSEL, which is expected to give the main contribution.

The pulse formation simulation for the "128 fs input parameters" (Table 1, Fig. 8) not only agrees with the pulse duration of 128 fs, but also with the spectral bandwidth of 9.5 nm (measured 9.48 nm) and the average output power of 78 mW (measured 80 mW). The 96 fs input parameters (Table 1) with the dispersion adapted to fit the compressed 96 fs pulses (Table 1: −12 fs^2 and −500 fs^3) results in negatively chirped 130 fs output pulses (i.e., not the measured 107 fs), which can be compressed with 1350 fs^2 positive GDD to 96 fs, a spectral bandwidth of 17.5 nm, and an average output power of 104 mW. With a slightly different cavity round-trip GDD of −4 fs^2 and TOD of −600 fs^3, we can fit the 107 fs output pulses: the simulation results in negatively chirped 108 fs output pulses, which can be compressed with 1350 fs^2 positive GDD to 86 fs (i.e., not the measured 96 fs), a spectral bandwidth of 17.4 nm, and an average output power of 100 mW (measured: 107 fs, 96 fs, 17.5 nm, 100 mW). Higher order dispersion of the ZnSe plate has not been taken into account. The agreement is no longer perfect, but the simulation confirms the 100 fs pulse duration with initially negatively chirped output pulses. At this point, we did not include the nonlinear induced absorption in the SESAM and VECSEL even though this becomes more important with shorter pulses.

Using the 128 fs input parameters (Table 1), we further explored the sensitivity of the cavity round-trip dispersion taking into account both the second-order dispersion (GDD) and the TOD. Different values of TOD are applied in addition to the GDD, centered around the lasing frequency (Fig. 8), with the cross indicating the dispersion values used for fitting the "128 fs result." The shortest pulses (101 fs) are achieved with 2 fs^2 GDD and 560 fs^3 TOD. The highest pulse peak power is 480 W and is obtained with 3 fs^2 GDD and 400 fs^3 TOD. Similar sensitivity is observed with the 96 fs input parameters, but is not shown here.

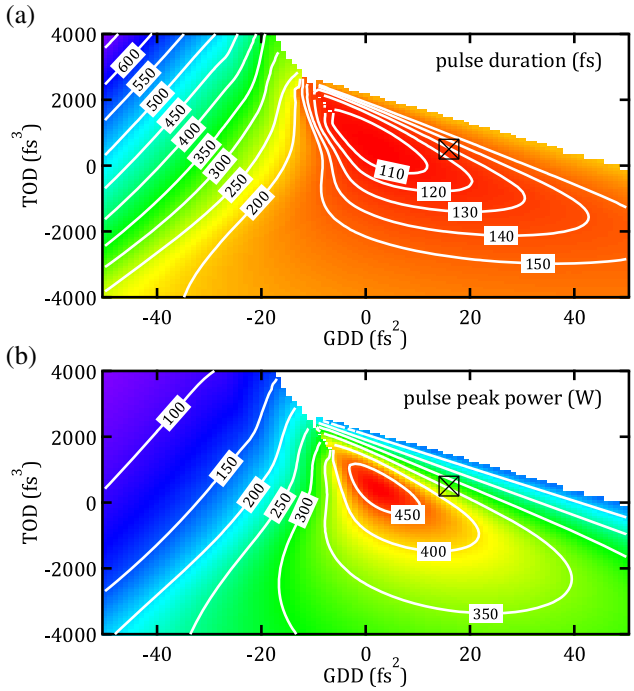

Fig. 8. Numerical pulse formation simulations using the 128 fs input parameters from Table 1. Cavity round-trip dispersion management for both (a) a shorter pulse duration and (b) a higher peak power as functions of second-order dispersion (i.e., GDD) and TOD is shown. The best performance is obtained in the red shaded area, and the "128 fs result" is marked with a black cross.

6. PERFORMANCE SCALING

From our simulations as presented in Section 5 we can conclude that the shortest pulse duration is mainly determined by the gain bandwidth, the gain saturation fluence, and the second- and third-order dispersion of the VECSEL. Figure 8 summarizes the general sensitivity on second- and third-order dispersion for both shorter pulse durations [red area in Fig. 8(a)] and higher pulse peak powers [red area in Fig. 8(b)]. Slightly positive TOD is needed for the shortest pulses. Too much positive TOD, however, causes instabilities, while negative TOD results in stable modelocking with slowly increasing pulse duration and decreasing peak power (Fig. 8). Negative GDD should be avoided, as the pulse duration increases rapidly into the picosecond regime, while for positive GDD, the pulse duration increases more slowly. Thus dispersion management becomes even more critical for broadband gain. Most recently, this has also been confirmed by Head *et al.* [35]. Control of the GDD and TOD of a VECSEL is challenging, as they are very sensitive to growth and fabrication uncertainties. Even growth errors in the 1% range can significantly change the wavelength-dependent dispersion. The simulation and the modelocking results confirm that a VECSEL gain bandwidth of 50–57 nm (FWHM) is sufficient for the generation of sub-100-fs pulses.

In the future we will focus our efforts toward even higher average output power and higher optical-to-optical efficiency of sub-100-fs SESAM modelocked VECSELs. The optimized broadband gain has been the key enabler for these new milestone results and has been achieved with flat field intensity enhancement, broadband dispersion control, and high-quality epitaxial

growth. Higher gain saturation fluence would further increase the output power and simultaneously shorten the pulse duration. The measured saturation fluences [Fig. 7(b)] have been lower than expected in comparison to [37] with the corresponding field intensity enhancement factors taken into account. However, we changed the lasing wavelength (1030 nm instead of 960 nm) and the epitaxial growth (MOVPE instead of MBE), which makes a direct comparison more difficult.

7. CONCLUSION

In conclusion, we have presented a significant improvement of SESAM modelocked VECSELs with both shorter pulse durations and higher average power with 96 fs pulses and 560 W pulse peak power. We performed a detailed characterization of both the VECSEL and the SESAM parameters, which were used as input parameters in our simulations (Table 1). We obtained good agreement between experiment and theory. Both second- and third-order dispersion management is required for short pulse durations and transform-limited pulses. The "128 fs result" is very close to transform limited with a time–bandwidth product of 1.09 times the ideal value. The 96 fs pulses were obtained by additional external dispersion compensation with a single path through a 2-mm-thick zinc selenide plate and are still not transform limited, with a time–bandwidth product of 1.47 times the ideal value of a sech^2 pulse shape. The bandwidth could in principle support transform-limited pulses as short as 65 fs. We have explained the sensitivity and importance of dispersion management and outlined design guidelines for future improvements in output power. With these record modelocking results, we have demonstrated that high-power 100 fs pulses are possible from optically pumped ultrafast VECSELs. This performance will enable octave-spanning supercontinuum generation without any additional external pulse amplifications based on recent progress with Si_3N_4 waveguides [27,28] for supercontinuum generation.

Funding. Swiss Confederation Program Nano-Tera.ch.

Acknowledgment. We thank the technology and cleanroom facility FIRST of ETH Zürich for advanced micro- and nanotechnology. This work was financed by the Swiss Confederation Program Nano-Tera.ch, which was scientifically evaluated by the Swiss National Science Foundation (SNSF).

REFERENCES

1. U. Keller and A. C. Tropper, "Passively modelocked surface-emitting semiconductor lasers," Phys. Rep. **429**, 67–120 (2006).
2. U. Keller, K. J. Weingarten, F. X. Kärtner, D. Kopf, B. Braun, I. D. Jung, R. Fluck, C. Hönninger, N. Matuschek, and J. Aus der Au, "Semiconductor saturable absorber mirrors (SESAMs) for femtosecond to nanosecond pulse generation in solid-state lasers," IEEE J. Sel. Top. Quantum Electron. **2**, 435–453 (1996).
3. B. W. Tilma, M. Mangold, C. A. Zaugg, S. M. Link, D. Waldburger, A. Klenner, A. S. Mayer, E. Gini, M. Golling, and U. Keller, "Recent advances in ultrafast semiconductor disk lasers," Light Sci. Appl. **4**, e310 (2015).
4. M. Kuznetsov, F. Hakimi, R. Sprague, and A. Mooradian, "High-power (>0.5-W CW) diode-pumped vertical-external-cavity surface-emitting semiconductor lasers with circular TEM_{00} beams," IEEE Photon. Technol. Lett. **9**, 1063–1065 (1997).
5. S. H. Park, J. Kim, H. Jeon, T. Sakong, S. N. Lee, S. Chae, Y. Park, C. H. Jeong, G. Y. Yeom, and Y. H. Cho, "Room-temperature GaN vertical-cavity surface-emitting laser operation in an extended cavity scheme," Appl. Phys. Lett. **83**, 2121–2123 (2003).
6. M. Rahim, M. Arnold, F. Felder, K. Behfar, and H. Zogg, "Midinfrared lead-chalcogenide vertical external cavity surface emitting laser with 5 μm wavelength," Appl. Phys. Lett. **91**, 151102 (2007).
7. T. L. Wang, Y. Kaneda, J. M. Yarborough, J. Hader, J. V. Moloney, A. Chernikov, S. Chatterjee, S. W. Koch, B. Kunert, and W. Stolz, "High-power optically pumped semiconductor laser at 1040 nm," IEEE Photon. Technol. Lett. **22**, 661–663 (2010).
8. B. Rudin, A. Rutz, M. Hoffmann, D. J. H. C. Maas, A.-R. Bellancourt, E. Gini, T. Südmeyer, and U. Keller, "Highly efficient optically pumped vertical emitting semiconductor laser with more than 20 W average output power in a fundamental transverse mode," Opt. Lett. **33**, 2719–2721 (2008).
9. A. Laurain, C. Mart, J. Hader, J. V. Moloney, B. Kunert, and W. Stolz, "15 W single frequency optically pumped semiconductor laser with sub-megahertz linewidth," IEEE Photon. Technol. Lett. **26**, 131–133 (2014).
10. B. Heinen, T. L. Wang, M. Sparenberg, A. Weber, B. Kunert, J. Hader, S. W. Koch, J. V. Moloney, M. Koch, and W. Stolz, "106 W continuous-wave output power from vertical-external-cavity surface-emitting laser," Electron. Lett. **48**, 516–517 (2012).
11. M. Mangold, M. Golling, E. Gini, B. W. Tilma, and U. Keller, "Sub-300-femtosecond operation from a MIXSEL," Opt. Express **23**, 22043–22059 (2015).
12. I. Kilen, J. Hader, J. V. Moloney, and S. W. Koch, "Ultrafast nonequilibrium carrier dynamics in semiconductor laser mode locking," Optica **1**, 192–197 (2014).
13. P. Klopp, U. Griebner, M. Zorn, and M. Weyers, "Pulse repetition rate up to 92 GHz or pulse duration shorter than 110 fs from a mode-locked semiconductor disk laser," Appl. Phys. Lett. **98**, 071103 (2011).
14. A. H. Quarterman, K. G. Wilcox, V. Apostolopoulos, Z. Mihoubi, S. P. Elsmere, I. Farrer, D. A. Ritchie, and A. Tropper, "A passively mode-locked external-cavity semiconductor laser emitting 60-fs pulses," Nat. Photonics **3**, 729–731 (2009).
15. K. G. Wilcox, A. C. Tropper, H. E. Beere, D. A. Ritchie, B. Kunert, B. Heinen, and W. Stolz, "4.35 kW peak power femtosecond pulse mode-locked VECSEL for supercontinuum generation," Opt. Express **21**, 1599–1605 (2013).
16. C. J. Saraceno, F. Emaury, C. Schriber, M. Hoffmann, M. Golling, T. Südmeyer, and U. Keller, "Ultrafast thin-disk laser with 80 μJ pulse energy and 242 W of average power," Opt. Lett. **39**, 9–12 (2014).
17. C. A. Zaugg, A. Klenner, O. D. Sieber, M. Golling, B. W. Tilma, and U. Keller, "Sub-100 MHz passively modelocked VECSEL," in *Conference on Lasers and Electro Optics (CLEO)* (Optical Society of America, 2013), paper CW1G.6.
18. M. Butkus, E. A. Viktorov, T. Erneux, C. J. Hamilton, G. Maker, G. P. A. Malcolm, and E. U. Rafailov, "85.7 MHz repetition rate mode-locked semiconductor disk laser: fundamental and soliton bound states," Opt. Express **21**, 25526–25531 (2013).
19. M. Hoffmann, Y. Barbarin, D. J. H. C. Maas, M. Golling, I. L. Krestnikov, S. S. Mikhrin, A. R. Kovsh, T. Südmeyer, and U. Keller, "Modelocked quantum dot vertical external cavity surface emitting laser," Appl. Phys. B **93**, 733–736 (2008).
20. M. Hoffmann, O. D. Sieber, V. J. Wittwer, I. L. Krestnikov, D. A. Livshits, Y. Barbarin, T. Südmeyer, and U. Keller, "Femtosecond high-power quantum dot vertical external cavity surface emitting laser," Opt. Express **19**, 8108–8116 (2011).
21. R. Bek, G. Kersteen, H. Kahle, T. Schwarzbäck, M. Jetter, and P. Michler, "All quantum dot mode-locked semiconductor disk laser emitting at 655 nm," Appl. Phys. Lett. **105**, 082107 (2014).
22. R. Aviles-Espinosa, G. Filippidis, C. Hamilton, G. Malcolm, K. J. Weingarten, T. Südmeyer, Y. Barbarin, U. Keller, S. I. C. O. Santos, D. Artigas, and P. Loza-Alvarez, "Compact ultrafast semiconductor disk laser: targeting GFP based nonlinear applications in living organisms," Biomed. Opt. Express **2**, 739–747 (2011).
23. C. A. Zaugg, A. Klenner, M. Mangold, A. S. Mayer, S. M. Link, F. Emaury, M. Golling, E. Gini, C. J. Saraceno, B. W. Tilma, and U. Keller, "Gigahertz self-referenceable frequency comb from a semiconductor disk laser," Opt. Express **22**, 16445–16455 (2014).
24. A. Klenner, S. Schilt, T. Südmeyer, and U. Keller, "Gigahertz frequency comb from a diode-pumped solid-state laser," Opt. Express **22**, 31008–31019 (2014).

25. A. H. Quarterman, L. E. Hooper, P. J. Mosley, and K. G. Wilcox, "Gigahertz pulse source by compression of mode-locked VECSEL pulses coherently broadened in the normal dispersion regime," Opt. Express **22**, 12096–12101 (2014).
26. H. R. Telle, G. Steinmeyer, A. E. Dunlop, J. Stenger, D. H. Sutter, and U. Keller, "Carrier-envelope offset phase control: a novel concept for absolute optical frequency measurement and ultrashort pulse generation," Appl. Phys. B **69**, 327–332 (1999).
27. A. Klenner, A. S. Mayer, A. R. Johnson, K. Luke, M. R. E. Lamont, Y. Okawachi, M. Lipson, A. L. Gaeta, and U. Keller, "Gigahertz frequency comb offset stabilization based on supercontinuum generation in silicon nitride waveguides," Opt. Express **24**, 11043–11053 (2016).
28. A. S. Mayer, A. Klenner, A. R. Johnson, K. Luke, M. R. E. Lamont, Y. Okawachi, M. Lipson, A. L. Gaeta, and U. Keller, "Frequency comb offset detection using supercontinuum generation in silicon nitride waveguides," Opt. Express **23**, 15440–15451 (2015).
29. C. Hönninger, R. Paschotta, F. Morier-Genoud, M. Moser, and U. Keller, "*Q*-switching stability limits of continuous-wave passive mode locking," J. Opt. Soc. Am. B **16**, 46–56 (1999).
30. A. Klenner and U. Keller, "All-optical *Q*-switching limiter for high-power gigahertz modelocked diode-pumped solid-state lasers," Opt. Express **23**, 8532–8544 (2015).
31. D. Hillerkuss, R. Schmogrow, T. Schellinger, M. Jordan, M. Winter, G. Huber, T. Vallaitis, R. Bonk, P. Kleinow, F. Frey, M. Roeger, S. Koenig, A. Ludwig, A. Marculescu, J. Li, M. Hoh, M. Dreschmann, J. Meyer, S. Ben Ezra, N. Narkiss, B. Nebendahl, F. Parmigiani, P. Petropoulos, B. Resan, A. Oehler, K. Weingarten, T. Ellermeyer, J. Lutz, M. Moeller, M. Huebner, J. Becker, C. Koos, W. Freude, and J. Leuthold, "26 Tbit s^{-1} line-rate super-channel transmission utilizing all-optical fast Fourier transform processing," Nat. Photonics **5**, 364–371 (2011).
32. M. Mangold, C. A. Zaugg, S. M. Link, M. Golling, B. W. Tilma, and U. Keller, "Pulse repetition rate scaling from 5 to 100 GHz with a high-power semiconductor disk laser," Opt. Express **22**, 6099–6107 (2014).
33. D. Waldburger, C. G. E. Alfieri, S. M. Link, E. Gini, M. Golling, M. Mangold, B. W. Tilma, and U. Keller, "Pulse shortening of an ultrafast VECSEL," Proc. SPIE **9734**, 973409 (2016).
34. O. D. Sieber, M. Hoffmann, V. J. Wittwer, M. Mangold, M. Golling, B. W. Tilma, T. Südmeyer, and U. Keller, "Experimentally verified pulse formation model for high-power femtosecond VECSELs," Appl. Phys. B **113**, 133–145 (2013).
35. C. R. Head, A. Hein, A. P. Turnbull, M. Polanik, E. A. Shaw, T. Chen Sverre, P. Unger, and A. C. Tropper, "High-order dispersion in sub-200-fs pulsed VECSELs," Proc. SPIE **9734**, 973408 (2016).
36. D. J. H. C. Maas, B. Rudin, A.-R. Bellancourt, D. Iwaniuk, S. V. Marchese, T. Südmeyer, and U. Keller, "High precision optical characterization of semiconductor saturable absorber mirrors," Opt. Express **16**, 7571–7579 (2008).
37. M. Mangold, V. J. Wittwer, O. D. Sieber, M. Hoffmann, I. L. Krestnikov, D. A. Livshits, M. Golling, T. Südmeyer, and U. Keller, "VECSEL gain characterization," Opt. Express **20**, 4136–4148 (2012).
38. G. J. Spühler, K. J. Weingarten, R. Grange, L. Krainer, M. Haiml, V. Liverini, M. Golling, S. Schon, and U. Keller, "Semiconductor saturable absorber mirror structures with low saturation fluence," Appl. Phys. B **81**, 27–32 (2005).
39. S. Hoogland, S. Dhanjal, A. C. Tropper, S. J. Roberts, R. Häring, R. Paschotta, and U. Keller, "Passively mode-locked diode-pumped surface-emitting semiconductor laser," IEEE Photon. Technol. Lett. **12**, 1135–1137 (2000).
40. A. Gosteva, M. Haiml, R. Paschotta, and U. Keller, "Noise-related resolution limit of dispersion measurements with white-light interferometers," J. Opt. Soc. Am. B **22**, 1868–1874 (2005).
41. I. Kilen, S. W. Koch, J. Hader, and J. V. Moloney, "Fully microscopic modeling of mode locking in microcavity lasers," J. Opt. Soc. Am. B **33**, 75–80 (2016).